Modeling by Numerical Reduction of Modes for Multivariable Control of an Optical-Fiber Draw Process

Kok-Meng Lee, *Fellow, IEEE*, Zhiyong Wei, and Zhi Zhou

Abstract—Motivated by a need for a method to derive practical and physical-based dynamic models that capture the essential characteristics of an optical-fiber draw process for precision control of diameter uniformity, we extend the Karhunen–Loeve decomposition technique with a Galerkin procedure to derive a reduced-order model (ROM) for a multivariable distributed-parameter system. We validated the ROM derived from a high-fidelity physics-based model by simulating a modern optical-fiber draw process, the numerical solutions for which have been experimentally verified in our earlier studies. Perturbation studies demonstrated that the 24th-order ROM agrees remarkably well with the original nonlinear semi-two-dimensional and quasi-one-dimensional distributed models. We further examine the efficiency of the ROM in the context of a model-based H_∞/LQG fiber drawing control system for the regulation of the fiber diameter and tension. The results show that variations in fiber diameter can be reduced significantly by appropriately distributing the number of retained eigenmodes among the physical state variables in the ROM. We also demonstrate that controlling the surrounding air temperature in addition to the draw speed is very effective in regulating both the fiber diameter and tension while simultaneously keeping the draw speed and temperature fluctuations to a minimum.

Note to Practitioners—Because of the stringent production requirements (on draw speed, tension, and temperature), diameter uniformity is a challenging distributed control problem in modern fiber production where progressively larger diameter preforms are drawn at higher speeds. The reduced-order model offers an effective way to observe physical variables in a multivariable distributed-parameter system, which may not be physically measured. While developed in the context of fiber diameter control, the modeling techniques presented in this paper are applicable to other material processing systems, such as deposition thickness control in semiconductor wafer manufacturing.

Index Terms—Distributed parameter systems, fiber draw process, H_∞/LQG, Karhunen–Loeve (K–L) decomposition, K–L Galerkin method, model-based control, optical fibers.

K.-M. Lee is with The George W. Woodruff School of Mechanical Engineering, Georgia Institute of Technology, Atlanta, GA 30332-0405 USA (e-mail: kokmeng.lee@me.gatech.edu).

Z. Wei is with the Analysis and Validation, New Technologies and Engine Component, Caterpillar, Mossville, IL 61552 USA (e-mail: Wei_Zhiyong@cat.com).

Z. Zhou is with the Center of Excellence for Control, Plug Power, Inc., Latham, NY 12110 USA (e-mail: zhi_zhou@plugpower.com).

I. INTRODUCTION

TO IMPROVE productivity and reduce setup cost in manufacturing optical fibers, modern draw towers must be able to draw fibers from large-diameter preforms at high speeds and yet be able to yield a high-quality product. One major obstacle of this trend is the difficulty in maintaining diameter uniformity, which influences transmission losses in the fiber and is directly related to manufacturing processes. During the drawing, the fiber diameter exhibits significant variations with spatial periods extending over a wide region along the fiber length. These problems become more pronounced with larger preforms and higher draw speeds.

Numerous investigations have been taken on the diameter control of the optical-fiber drawing process to minimize transmission losses. Nakahara *et al.* [1] studied the effects of different thermal and mechanical drawing conditions on the quality and tensile strength of the fibers. They concluded that temperature variation in the furnace is a major factor affecting the high-frequency fiber diameter fluctuations, and that low-frequency fluctuations are caused by longitudinal variations in the preform diameter. They suggested a feedback control of drawing speed to reduce low-frequency diameter variations. Smithgall [2] experimentally obtained an empirical transfer function (that relates the fiber diameter to draw speed) by heating a preform (7 to 25 mm in diameter), drawn at a nominal speed of 1 m/s, and measured the fiber diameter using an interference fringe counting technique (with an accuracy of 0.25 μm at a rate of 1000 measurements per second). Due to physical limitations, measurements made at some point below the heat zone were modeled as a transport delay (40 to 100 ms) to characterize the fiber diameter responding to geometrical variations in the molten neck-down region. Smithgall demonstrated that the standard deviation of fiber diameter can be significantly reduced using an optimization theory based on a mean-square-error criterion, and that the loop response is sensitive to the measurement delay. Imoto, *et al.* [3] studied the use of laminar gas flow to reduce the short-period variations of the fiber diameter due to rapidly changing factors, such as gas-flow instabilities, and in the furnace and/or mechanical vibration of the drawing machine. They experimentally demonstrated that controlling fast-response laminar gas flow around the surface of the converging glass could be more effective (than by simply varying the draw speed) to reduce the effects of high-frequency fluctuations on the fiber diameter since the draw speed is difficult to respond quickly due to the mechanical inertia of the rotating capstans/drums. Similar to those pub-

lished earlier, Imoto, *et al.* based their study on small diameter performs of 7.5 mm and drawn at a slow speed of 5 m/s. Mulpur and Thompson [4] applied model reference control and quasi-nonlinear control techniques on the diameter control based on an isothermal model. Since the isothermal model (that is highly simplified and generally neglects one or more terms among the advection, radiation, and conduction in the energy transfer) was open-loop unstable when the draw ratio exceeded some critical value, their control efforts focused on stabilizing the closed-loop system under a high draw ratio.

In the design of modern fiber draw towers, the trend is to draw optical fibers at high speeds (20 m/s or higher) from large-diameter preforms (0.08 m or larger) in order to improve productivity and product quality while reducing manufacturing cost. This imposes a challenge as the draw ratio is two or more orders of magnitude higher than that considered in the previous studies. Furthermore, the glass undergoes large temperature variations inside the furnace and the post chamber, which consequently affects the fiber velocity and diameter through the influence of glass viscosity, which is strongly temperature dependent. For these reasons, we have focused on developing methods to derive ROMs based on rigorous physical principles, which capture the dominant dynamics of the energy transports with the minimum order.

Modern fiber draw processes are represented as nonlinear distributed-parameter (NLDP) systems. Control of these processes is particularly challenging since practical dynamic models that can be implemented without undue complications are difficult to obtain. The degrees of freedom of NLDP systems are essentially infinite and often too complicated to be implemented in an industry. Coupled by a lack of satisfactory mathematical theory and design procedure of NLDP systems, most engineers rely on lumped-parameter techniques (that generally yield only first-order approximation) to model distributed parameter systems. The controllers so designed are often less than optimal for manufacturing processes (such as precision drawing of optical fibers), where practical in-situ measurements are difficult to make, particularly in real time. The model-based diameter control of fiber drawing processes requires the development of appropriate models. Tchikanda and Lee [5] developed a linear state-space model for the draw process by discretizing a quasi-one-dimensional (1-D) thermal fluid model using the finite-difference method resulting in a high-fidelity model (147th order). The fiber drawing process is described by the nonlinear parabolic partial-differential-equations (PDEs) which include convection and diffusion terms. The main feature of parabolic PDEs is that their dominant dynamic behavior is usually characterized by a finite (typically small) number of degrees of freedom [6]. This implies that the dominant dynamic behavior of such systems can be approximately described by the finite-dimensional ordinary differential equations (ODEs) using the Karhunen–Loeve (K–L) decomposition technique, which was originally devised as a rational technique enabling a stochastic field (ensembles or snapshots) to be represented with a minimum degree of freedom [7]. Contrary to the traditional Galerkin methods that employ trigonometric or other special functions as basis functions, the method introduced here uses empirical functions of the K–L

decomposition as basis functions in the Galerkin procedure in discretizing the PDEs. As the eigenfunctions represent the dominant physical characteristics of the system, the resulting ODEs have the minimum order for the required accuracy [8]. Recently, a number of researchers explore the use of the K–L Galerkin method to reduce thermal-fluid system models to a set of ODEs [9]–[15]. Most of these studies applied the K–L Galerkin method to control systems with a single distributed temperature variable for deposition thickness control in the thermal processing of wafers.

The remainder of this paper offers the following.

1) We present a nonlinear distributed-parameter quasi-1-D model to characterize a fiber draw process, upon which the perturbation model and a practical ROM are derived about the operating point. Together, with our earlier CFD models [16], [17], the different levels of models can be applied to design optimization, dynamic analysis, and performance prediction; thereby offering an effective means to reduce time and costly experiments in developing and implementing model-based control systems.

2) This paper represents the first detailed study in extending the K–L Galerkin method to a fiber draw process control characterized by more than one highly coupled distributed state variable, and involving heat inputs from the free surface (in the PDE) as well as mechanical inputs applied at the boundary conditions. We validate the K–L Galerkin method by simulating a modern fiber draw tower capable of drawing from large-diameter preforms at high speeds, and then comparing the results against experimentally verified numerical solutions.

3) We examine the efficiency of the ROM derived using the K–L Galerkin method in the context of model-based control. For this purpose, a H_∞/LQG controller is designed for regulating both the diameter and tension of optical fiber. Since the molten free-surface cannot be physically measured, the ROM offers an effective means to predict the glass geometry under heating; thereby eliminating control problems associated with the measurement lag in the feedback loop. As will be demonstrated, the ROM-based H_∞/LQG diameter-controlled system utilizing both the air temperature and draw speed as inputs is very effective in regulating fiber diameter and tension simultaneously while keeping the draw speed and temperature fluctuations to within 0.1 m/s and less than 1 °K, respectively.

II. PROCESS DESCRIPTION

The system considered here is a typical fiber draw process as shown in Fig. 1, where the fiber is drawn from a melting preform (or cylindrical glass rod) in a high-temperature furnace followed by cooling in the post chamber. The deviation of the fiber diameter must be kept within an acceptable tolerance. At the same time, the temperature variation of the fiber after leaving the post chamber must be minimized to avoid downgrading the subsequent coating process. As shown in Fig. 1, the controlling inputs are the feedrate of the preform, the draw speed of the fiber, and the heat transfer at the surface of the glass/fiber through
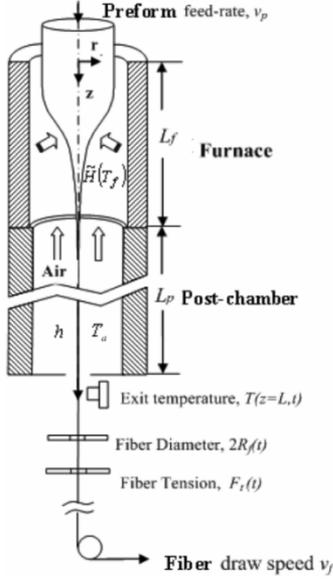
Fig. 1. Fiber draw process.

radiation and convection. The measurable outputs are the fiber diameter, temperature, and tension.

In [17], we have derived two computational models (semi-two-dimensional (2-D) and quasi-1-D) to describe the dynamics of the axisymmetrical glass flow from the laws of mass, momentum, and energy conservation. The fiber draw processes involves incompressible highly viscous fluid flow, where velocity variations in the radial direction are greatly reduced by the strong shear stresses. Thus, both models assume the velocity distribution is essentially 1-D. The semi-2-D model, which is solved numerically from the Navier–Stoke equations, provides a detailed description of the 2-D-temperature and 1-D velocity fields and is useful for process design. On the other hand, the quasi-1-D model (where the coefficients of the PDEs are radially integrated parameters derived from the solutions of the 2-D model) explicitly solves for the glass geometry, velocity, and temperature along the axial direction. In the interest to provide a simple yet practical formulation for deriving a more tractable model for the control of diameter uniformity, we derive the ROM from the nonlinear distributed quasi-1-D model that was based on the following assumptions: 1) the velocity and temperature variations in the radial direction are neglected; 2) the surface tension and the air-side normal stress are considered very small; 3) the total axial stress can be expressed using the elongation model [18].

In terms of the state vector

$$\mathbf{Q} = [a \quad v \quad T]^\mathrm{T}$$

where $a(z,t)$, $v(z,t)$, and $T(z,t)$ are the cross-sectional area of radius $R(z,t)$, axial velocity, and temperature of the glass, the dynamics of the quasi-1-D glass flow can be described by (1)

$$\mathbf{I}_m \left(\mathbf{\Gamma}_m \frac{\partial \mathbf{Q}}{\partial t} + \frac{\partial \mathbf{F}_c}{\partial z} \right) = \frac{\partial}{\partial z} \left(\mathbf{\Gamma} \frac{\partial \mathbf{Q}}{\partial z} \right) + \mathbf{S} \qquad (1)$$

where

$$\mathbf{F}_c = [av \quad av^2 \quad avT]^\mathrm{T};$$

$$\mathbf{S} = \left[0 \quad \rho g a \quad -2\pi R q'' + 3a\mu \left(\frac{\partial v}{\partial z} \right)^2 \right]^\mathrm{T};$$

$$\mathbf{I}_m = \mathrm{diag}(1 \quad \rho \quad \rho c_p);$$

$$\mathbf{\Gamma} = \mathrm{diag}(0 \quad 3a\mu \quad ak_{\mathrm{eq}});$$

$$\mathbf{\Gamma}_m = \begin{bmatrix} 1 & 0 & 0 \\ v & a & 0 \\ T & 0 & a \end{bmatrix}$$

and where q'' is the heat flux at the glass surface boundary; g is the gravitational acceleration; and k_{eq} is the equivalent thermal conductivity. For a semitransparent material

$$k_{\mathrm{eq}} = k_m + \widetilde{k}(T) \qquad (1a)$$

$\tilde{k}(T)$ is the apparent Rosseland's conductivity that accounts for the radiative transfer in the participating medium such as glass, and ρ, μ, k_m, and C_p are the density, viscosity, thermal conductivity, and specific heat of the glass, respectively.

The free surface of the glass preform in the fiber drawing process is heated by both radiation and air convection

$$q'' = q_r'' + q_c'' \qquad (1b)$$

where

$$q_r'' = \widetilde{\varepsilon}(\widetilde{E} - \widetilde{H}) \qquad (1c)$$

$$q_c'' = h(T - T_a) \qquad (1d)$$

$\tilde{\varepsilon}$ is the apparent emissivity, $\tilde{E}(T) = \sigma T^4$ is the total emissive power, $\tilde{H}(T)$ is the apparent irradiation from the furnace, h is the convective heat transfer coefficient, and T_a is the radially lumped air temperature.

In addition to the above heat inputs, two other manipulating inputs are the preform feedrate and the draw speed, which are specified boundary conditions given by

$$v(z = 0) = v_p(t) \qquad (2a)$$

$$v(z = L) = v_f(t). \qquad (2b)$$

III. DERIVATION OF A REDUCED ORDER MODEL

Equation (1) with its boundary conditions is referred here as a quasi-1D model since the parameters ($\tilde{H}$, h, T_a, and $\tilde{k}$) are derived from the steady-state solution of the original 2D equations. Once the parameters are defined, the state-space ROM can be derived using the following three steps.

1) Find the appropriate shape functions using the K–L decomposition.
2) Linearize the PDEs (1) and discretize the perturbed state variables using the Gelekin procedure with eigenfunctions obtained using K–L decomposition.
3) Along with the actuator and measurement equations, the complete set of state-space equations of a fiber draw system can then be derived.

A. Karhunen–Loeve (K–L) Decomposition

In order to obtain a finite-order model, we introduce the K–L decomposition technique to obtain the numerical eigenfunctions from the (2-D or quasi-1-D) simulation of the physical model as a basis set in the Galerkin procedure. The eigenfunctions thus have embedded physical characteristics and satisfy the boundary conditions automatically. For clarity, we introduce the K–L Galerkin procedure using the quasi-1-D model (1) in the following discussion.

The distributed state variables (a, v, and T) are sampled during the transient to all of the possible manipulating inputs and the disturbances. As these sampled physical variables have arbitrary shapes, they are often called irregularly shaped functions or snapshots. We select N snapshots $\{\eta_n(z)\}$ with $n = 1, 2, \ldots, N$ for each state variable. The essence of the K–L decomposition is to obtain the most typical or characteristic structure $\phi(z)$ among these snapshots. This is equivalent to obtaining $\phi(z)$ that minimizes the following objective function:

$$J = \frac{1}{N} \sum_{n=1}^{N} \int_0^L [\phi(z) - \eta_n(z)]^2 \, dz \tag{3}$$

for which we impose the following normalization condition on ϕ to make it unique:

$$\int_0^L \phi^2(z) dz = 1. \tag{4}$$

The minimization of the above cost function is mathematically equivalent to maximize the ensemble average of the inner product between $\phi(z)$ and $\eta_n(z)$

$$\text{Maximize } J = \frac{\frac{1}{N} \sum_{n=1}^{N} \left[\int_0^L \phi(z) \eta_n(z) dz \right]^2}{\int_0^L \phi^2(z) dz} \tag{5}$$

which can be rewritten as

$$\frac{1}{N} \sum_{n=1}^{N} \int_0^L \phi(z) \eta_n(z) dz \int_0^L \phi(z') \eta_n(z') dz'$$

or

$$\int_0^L [\mathbf{R}\phi(z)] \phi(z') dz'$$

where the linear operator $\mathbf{R}$ is defined as

$$\mathbf{R}\phi(z) = \int_0^L \left[\frac{1}{N} \sum_{n=1}^{N} \eta_n(z) \eta_n(z') \right] \phi(z) dz. \tag{6}$$

The maximization problem of (5) is thus reduced to the following eigenvalue problem:

$$\mathbf{R}\phi = \lambda \phi. \tag{7}$$

The function that maximizes J is the eigenfunction of (7), corresponding to the largest eigenvalue. Expressing ϕ as a linear combination of the snapshots [19]

$$\phi(z) = \sum_{n=1}^{N} c_n \eta_n(z) \tag{8}$$

and substituting it into (7), the most typical characteristic structure $\phi(z)$ among the snapshots $\{\eta_n(z)\}$ is equivalent to solving the following eigenvalue problem [12]:

$$\mathbf{B}\mathbf{c} = \lambda \mathbf{c} \tag{9}$$

where the entry of matrix $\mathbf{B}$ is

$$B^{\kappa k} = \frac{1}{N} \int_0^L \eta_\kappa(z) \eta_k(z) dz. \tag{10}$$

The eigenvector $\mathbf{c} = [c_1 \cdots c_N]^{\mathrm{T}}$ is then substituted into (8) to generate the eigenfunctions. Since the matrix $\mathbf{B}$ is symmetric and positive-definite, the eigenfunctions also satisfy the following orthogonality relationship:

$$\int_0^L \phi_i(z) \phi_j(z) dz = 0 \quad if \ i \neq j. \tag{11}$$

We denote the eigenvalues ($\lambda_1 > \lambda_2 > \ldots > \lambda_N$) and their corresponding eigenfunctions ($\phi_1, \phi_2, \ldots, \phi_N$) in the order of magnitude of eigenvalues, that is, the eigenfunction ϕ_1 (corresponding to λ_1) is the most typical structure of the snapshots $\{\eta_n(z)\}$ followed by $\phi_2, \ldots, \phi_N$ and so forth.

B. Perturbation Model

In deriving the perturbation model about a steady-state operating condition

$$\overline{Q} = \begin{bmatrix} \overline{a}(z) & \overline{v}(z) & \overline{T}(z) \end{bmatrix}^{\mathrm{T}} \tag{12a}$$

which can be solved numerically from the PDEs characterizing the glass flow [16], [17], we define the (dimensionless) perturbation state vector as

$$\hat{Q} = [\hat{a} \quad \hat{v} \quad \hat{T}]^{\mathrm{T}} \tag{12b}$$

where $\hat{a} = (a - \overline{a})/\overline{a}$, $\hat{v} = (v - \overline{v})/\overline{v}$, and $\hat{T} = (T - \overline{T})/\overline{T}$. The nonlinear temperature dependency of the parameters $\mu(T)$, $k_{eq}(T)$, and $\tilde{E}(T)$ is approximated by the following linear relations:

$$\mu(T) = \overline{\mu}(\overline{T}) + \left(\frac{d\mu}{dT} \right)\bigg|_{\overline{T}} \overline{T}\hat{T} \tag{13a}$$

$$k_{eq}(T) = \overline{k}(\overline{T}) + \left(\frac{dk_{eq}}{dT} \bigg| \right)_{\overline{T}} \overline{T}\hat{T} \tag{13b}$$

and

$$\widetilde{E}(T) = \overline{E}(\overline{T}) + \left(\frac{d\tilde{E}}{dT} \right)\bigg|_{\overline{T}} \overline{T}\hat{T}. \tag{13c}$$

In addition, we account for the fluctuations in the surface heat flux as follows:

$$\hat{q}(z, t) = q''(z, t) - \overline{q}(z) = k_T \hat{T} + \mathbf{k}_u \mathbf{u}_q + \mathbf{k}_w \mathbf{w}_1 \tag{14}$$

where $\overline{q}$ is the value of q'' at the operating point; the vector

$$\mathbf{u}_q = [\hat{T}_f \quad \hat{T}_a]^{\mathrm{T}} \tag{14a}$$

characterizes the furnace and air temperatures $\hat{T}_f$ and $\hat{T}_a$ for manipulating the radiation and air convection, respectively; and

$$\mathbf{w}_1 = [w_f \quad w_h]^{\mathrm{T}} \tag{14b}$$

describes the disturbances in T_f and in h. The coefficients (k_T, $\mathbf{k}_u$, and $\mathbf{k}_w$) are derived by linearizing (1c) and (1d)

and

$$\hat{q}_r = \left(\tilde{\varepsilon} \left. \frac{\partial \widetilde{E}}{\partial T} \right|_{\overline{T}} \overline{T} \right) \hat{T} - \tilde{\varepsilon} \overline{H} \left. \frac{\partial \widetilde{H}}{\partial T_f} \right|_{\overline{T}_f} (\hat{T}_f + w_f)$$

$$\hat{q}_c = \overline{hT}\hat{T} - \overline{hT_a}\hat{T}_a + \overline{h}(\overline{T} - \overline{T}_a)w_h.$$

Along with (1b), the coefficients in (14) can be identified as

$$k_T = \overline{hT} + \tilde{\varepsilon} \left. \frac{\partial \widetilde{E}}{\partial T} \right|_{\overline{T}} \overline{T} \tag{14c}$$

$$\mathbf{k}_u = \left[-\tilde{\varepsilon}\overline{H} \left. \frac{\partial \widetilde{H}}{\partial T_f} \right|_{\overline{T}_f} \quad -\overline{hT_a} \right] \tag{14d}$$

$$\mathbf{k}_w = \left[-\tilde{\varepsilon}\overline{H} \left. \frac{\partial \widetilde{H}}{\partial T_f} \right|_{\overline{T}_f} \quad \overline{h}(\overline{T} - \overline{T}_a) \right]. \tag{14e}$$

Using (12)–(14), the perturbation model about $\overline{Q}$ can be shown to be

$$\overline{\mathbf{m}} \frac{\partial \hat{\mathbf{Q}}}{\partial t} = -\frac{\partial}{\partial z}[\overline{\mathbf{\Lambda}}\hat{\mathbf{Q}}] + \frac{\partial}{\partial z}\left(\overline{\mathbf{\Gamma}_1}\hat{\mathbf{Q}} + \overline{\mathbf{\Gamma}_2}\frac{\partial \hat{\mathbf{Q}}}{\partial z} \right) + \overline{\mathbf{S}}\hat{\mathbf{Q}} + \overline{\mathbf{b}}u_q + \overline{\mathbf{c}}\mathbf{w}_1 \tag{15}$$

where

$$\overline{\mathbf{m}} = \overline{a} \begin{bmatrix} 1 & 0 & 0 \\ \rho\overline{v} & \rho\overline{v} & 0 \\ \rho C_p\overline{T} & 0 & \rho C_p\overline{T} \end{bmatrix};$$

$$\overline{\mathbf{\Lambda}} = \overline{av} \begin{bmatrix} 1 & 1 & 0 \\ \frac{1}{\rho\overline{v}} & 2\rho\overline{v} & 0 \\ \rho C_p\overline{T} & \rho C_p\overline{T} & \rho C_p\overline{T} \end{bmatrix};$$

$$\overline{\mathbf{\Gamma}_1} = \overline{a} \begin{bmatrix} 0 & 0 & 0 \\ 3\overline{\mu}\left(\frac{d\overline{v}}{dz}\right) & 3\overline{\mu}\left(\frac{d\overline{v}}{dz}\right) & 3\left(\frac{d\overline{v}}{dz}\right)\left(\frac{d\mu}{dz}\right)\Big|_{\overline{T}}\overline{T} \\ \overline{k}\left(\frac{d\overline{T}}{dz}\right) & 0 & \left(\frac{d\overline{T}}{dz}\right)\left[\overline{k} + \left(\frac{d\tilde{k}}{dz}\right)\Big|_{\overline{T}}\right]\overline{T} \end{bmatrix};$$

$$\overline{\mathbf{\Gamma}_2} = diag(0 \quad 3\overline{av\mu} \quad \overline{akT});$$

$$\overline{\mathbf{S}} = \begin{bmatrix} 0 & 0 & 0 \\ \rho g\overline{a} & 0 & 0 \\ \overline{s}_1 & \overline{s}_2 & \overline{s}_3 \end{bmatrix};$$

$$\overline{s}_1 = \frac{\pi\overline{R}\overline{q}}{\mathbf{n}\bullet\mathbf{r}} + 3\overline{a\mu}\left(\frac{d\overline{v}}{dz}\right)^2;$$

$$\overline{s}_2 = 6\overline{a\mu}\left(\frac{d\overline{v}}{dz}\right)^2 + 2\overline{av\mu}\frac{d\overline{v}}{dz}\frac{\partial}{\partial z};$$

$$\overline{s}_3 = \frac{-2\pi\overline{RT}}{\mathbf{n}\bullet\mathbf{r}}k_T + 3\overline{aT}\left(\frac{d\overline{v}}{dz}\right)^2\left.\frac{d\mu}{dT}\right|_{\overline{T}};$$

$$\overline{\mathbf{b}} = \begin{bmatrix} 0 & 0 & \frac{2\pi\overline{R}}{\mathbf{n}\bullet\mathbf{r}}\mathbf{k}_u^{\mathrm{T}} \end{bmatrix}^{\mathrm{T}};$$

and

$$\overline{\mathbf{c}} = \begin{bmatrix} 0 & 0 & \frac{2\pi\overline{R}}{\mathbf{n}\bullet\mathbf{r}}\mathbf{k}_w^{\mathrm{T}} \end{bmatrix}^{\mathrm{T}}.$$

The state variables $\hat{a}(z,t)$, $\hat{v}(z,t)$, and $\hat{T}(z,t)$ in the linear PDEs are distributed and, thus, the dimension of (15) is essentially infinite.

C. Galerkin's Procedure

A Galerkin procedure employing the above numerical eigenfunctions as a basis set can then be applied to (15), which leads to a set of linear ODEs. For this, we define the perturbed state variables in (12b) as a combination of the numerical eigenfunctions. As derived in Section II, two of the manipulating inputs: the preform feedrate $\hat{v}_p(t)$ and the fiber draw speed $\hat{v}_f(t)$ are specified as boundary values in (2). To ease the controller design, we explicitly define the feedrate and draw speed as system inputs

$$\hat{a}(z,t) \hat{=} \sum_{i=1}^{N_a} x_{ai}(t)\phi_{ai}(z) \tag{16a}$$

$$\hat{v}(z,t) = \sum_{i=1}^{N_v} x_{vi}(t)\phi_{vi}(z) + \frac{\overline{v}_{f\alpha}}{\alpha_f}\hat{v}_f(t) + \frac{\overline{v}_{p\alpha}}{\alpha_p}\hat{v}_p(t) \tag{16b}$$

$$\hat{T}(z,t) \hat{=} \sum_{i=1}^{N_T} x_{Ti}(t)\phi_{Ti}(z) \tag{16c}$$

where $\overline{v}_{f\alpha}$ and $\overline{v}_{p\alpha}$ are the steady-state responses to a small step change in $\hat{v}$ at the boundaries with magnitude α_f and α_p, respectively; and N_a, N_v, and N_T are the number of eigenfunctions retained in the expansion of $\hat{a}$, $\hat{v}$, and $\hat{T}$, respectively. Note that the first term on the right-hand side of (16b) satisfies homogeneous boundary conditions.

We substitute (16a)–(c) into (15) followed by applying the Galerkin procedure. The procedure involves multiplying (15) by $\mathbf{\Phi}_k$ and then integrating both sides of the resulting equation with respect to z, where

$$\mathbf{\Phi}_k = \mathrm{diag}(\phi_{ak} \quad \phi_{vk} \quad \phi_{Tk}). \tag{17}$$

The resulting equations for the glass flow can be written using state-space representation. For $N_a = N_v = N_T = N$

$$\sum_{i=1}^{N}(\mathbf{M}_{ki}\dot{\boldsymbol{\chi}}_i) = \sum_{i=1}^{N}(\mathbf{E}_{ki}\boldsymbol{\chi}_i) + \mathbf{F}_k\mathbf{x}_A + \mathbf{G}_k\dot{\mathbf{x}}_A + \mathbf{H}_k\mathbf{w}_1 \tag{18}$$

where $k = 1,\ldots,N$

$$\boldsymbol{\chi}_i = [x_{ai} \quad x_{vi} \quad x_{Ti}]^{\mathrm{T}}; \quad \mathbf{x}_A = [\hat{v}_f \quad \hat{v}_p \quad \mathbf{u}_q^{\mathrm{T}}]^{\mathrm{T}};$$

$$\mathbf{M}_{ki} = \int_0^L \mathbf{\Phi}_k\overline{\mathbf{m}}\mathbf{\Phi}_i dz;$$

$$\mathbf{E}_{ik} = \int_0^L \mathbf{\Phi}_k\left\{ \frac{d}{dz}\left[(-\overline{\mathbf{\Lambda}} + \overline{\mathbf{\Gamma}}_1)\mathbf{\Phi}_i + \overline{\mathbf{\Gamma}}_2\frac{d\mathbf{\Phi}_i}{dz}\right] + \overline{\mathbf{S}}\mathbf{\Phi}_i \right\}dz$$

$$\mathbf{F}_k = \int_0^L \mathbf{\Phi}_k\left\{ \begin{array}{l} \frac{d}{dz}\left[(-\overline{\mathbf{\Lambda}} + \mathbf{\Gamma}_1)\mathbf{V}_\alpha + \mathbf{\Gamma}_2\frac{d\mathbf{V}_\alpha}{dz}\right] + \overline{\mathbf{S}}\mathbf{V}_\alpha + \\ \mathrm{diag}\left(0 \quad 0 \quad \frac{2\pi\overline{R}}{\mathbf{n}\bullet\mathbf{r}}\tilde{\varepsilon}\overline{H}\right) \end{array} \right\}dz$$

$$\mathbf{G}_k = \int_0^L \mathbf{\Phi}_k\overline{av}\mathbf{V}_\alpha dz; \quad \mathbf{H}_k = -\int_0^L \mathbf{\Phi}_k\overline{\mathbf{c}}dz;$$

and

$$\mathbf{V}_\alpha = \mathrm{diag}\left(\frac{\overline{v}_{f\alpha}}{\alpha_f} \quad \frac{\overline{v}_{p\alpha}}{\alpha_p} \quad 0 \right).$$

D. State-Space Representation

For completeness, we derive the state-space representation for the overall system that includes the ROM characterizing the glass flow, the actuator dynamics, and the measurements. The actuator dynamics of the inputs to the system represented by (18) are typically first order

$$\dot{\mathbf{x}}_A = \mathbf{A}_A \mathbf{x}_A + \mathbf{B}_A \mathbf{u} \qquad (19)$$

where

$$\mathbf{u} = \begin{bmatrix} u_f & u_p & u_T & u_a \end{bmatrix}^{\mathrm{T}}. \qquad (19a)$$

The elements of $\mathbf{u}$ are the electrical inputs to the pre-form-feeding motor, fiber-drawing motor, furnace, and air-temperature controller, respectively

$$\mathbf{A}_A = \mathrm{diag} \left(\frac{1}{\tau_f} \quad \frac{1}{\tau_p} \quad \frac{1}{\tau_T} \quad \frac{1}{\tau_a} \right) \qquad (19b)$$

and

$$\mathbf{B}_A = \mathrm{diag} \left(\frac{K_f}{\tau_f} \quad \frac{K_p}{\tau_p} \quad \frac{K_T}{\tau_T} \quad \frac{K_a}{\tau_a} \right) \qquad (19c)$$

where τ and K are the time constant and gain of the actuators, respectively.

The measurable outputs include the fiber cross-sectional area, temperature, and tension at the post-chamber exit $(z = L)$

$$\mathbf{y} = \begin{bmatrix} \hat{a}(L,t) & \hat{T}(L,t) & \hat{F}(L,t) \end{bmatrix}^{\mathrm{T}} \qquad (20)$$

where $\hat{a}$ and $\hat{T}$ are given by (16a) and (16c), respectively. Using the elongation model $F_t = 3a\mu dv/dz$, the perturbation form of the tension force can be shown to be

$$\hat{F} = \mathbf{C}_F^{\mathrm{T}} \boldsymbol{\chi} \qquad (21)$$

where

$$\mathbf{C}_F = [\phi_{a1} \quad c_v \phi_{v1} \quad c_\mu \phi_{T1}; \quad \ldots;$$
$$\phi_{aN} \quad c_v \phi_{vN} \quad c_\mu \phi_{TN}]|_{z=L};$$
$$c_v = \left(1 + \overline{v} \frac{d}{d\overline{v}} \right); \quad c_\mu = \frac{1}{\mu} \left. \frac{d\mu}{dT} \right|_{\overline{T}};$$

and

$$\boldsymbol{\chi} = \begin{bmatrix} \boldsymbol{\chi}_1^{\mathrm{T}} & \boldsymbol{\chi}_2^{\mathrm{T}} & \cdots & \boldsymbol{\chi}_N^{\mathrm{T}} \end{bmatrix}^{\mathrm{T}}.$$

As described earlier, the eigenfunctions are arranged in the order of the typical structure of the snapshots; the properties of the empirical eigenfunctions as well as the number of terms to be retained can be examined numerically by comparing the ROM with the CFD model. As will be seen in the results, the system order obtained using the K–L Galerkin method is usually small. The state-space representation of the overall system thus takes the following form:

$$\dot{\mathbf{x}}_0 = \mathbf{A}_0 \mathbf{x}_0 + \mathbf{B}_0 \mathbf{u} + \mathbf{D}_0 \mathbf{w}_1$$
$$\mathbf{y} = \mathbf{C}_0 \mathbf{x}_0 \qquad (22)$$

where $\mathbf{x}_0 = [\boldsymbol{\chi}^{\mathrm{T}} \quad \mathbf{x}_A^{\mathrm{T}}]^{\mathrm{T}}$; $\mathbf{A}_0 \in \mathbf{R}^{K \times K}$, $\mathbf{B}_0 \in \mathbf{R}^{K \times 4}$, $\mathbf{C}_0 \in \mathbf{R}^{3 \times K}$, $\mathbf{D}_0 \in \mathbf{R}^{K \times 2}$, and $K = N_a + N_v + N_T + 4$.

For $N_a = N_v = N_T = N$, the system matrixes are readily obtained from (18)–(21), which takes the form

$$\mathbf{A}_0 = \begin{bmatrix} \mathbf{M}^{-1}\mathbf{E} & \mathbf{F} + \mathbf{G}\mathbf{A}_A \\ 0^{4 \times 3N} & \mathbf{A}_A \end{bmatrix} \qquad (22a)$$

$$\mathbf{B}_0 = \begin{bmatrix} \mathbf{G}\mathbf{B}_A \\ \mathbf{B}_A \end{bmatrix} \qquad (22b)$$

$$\mathbf{C}_0 = \begin{bmatrix} \phi_{a1} \, 0 \, 0, \, \ldots \, \phi_{aN} \, 0 \, 0, \, 0^{1 \times 4} \\ 0 \, 0 \, \phi_{T1}, \, \ldots \, 0 \, 0 \, \phi_{TN}, \, 0^{1 \times 4} \\ \mathbf{C}_F^{\mathrm{T}} \end{bmatrix}_{z=L} \qquad (22c)$$

$$\mathbf{D}_0 = \begin{bmatrix} \mathbf{H} \\ 0^{4 \times 2} \end{bmatrix} \qquad (22d)$$

where the elements of $\mathbf{M}$ and $\mathbf{E}$ are $\mathbf{M}_{\mathrm{ki}}$ and $\mathbf{E}_{\mathrm{ki}}$, respectively; and $\mathbf{F}$, $\mathbf{G}$, and $\mathbf{H}$ are constructed by $\mathbf{F}_{\mathrm{k}}$, $\mathbf{G}_{\mathrm{k}}$, and $\mathbf{H}_{\mathrm{k}}$ in the column direction, respectively.

The remainder of the results is broadly divided into two parts–model verification and illustrative control applications–which are discussed in Sections IV and V, respectively.

IV. MODEL VALIDATION

A MATLAB program with C++ subroutines has been written to simulate the dynamic responses of a modern optical-fiber drawing process so that the ROM can be validated against the solutions of the original quasi-1-D and semi-2-D models, which have been validated experimentally in [17]. The values of the parameters used in the simulation are given in Table I.

A. Parameters for Quasi-1-D Model

The temperature and velocity fields at steady-state were computed from the semi-2-D model with a grid number $(z \times r)$ of 200×15, which provides a basis for deriving the perturbation model and computing the distributed parameters in the quasi-1-D model. The temperatures of the glass, surrounding air, and furnace/post-chamber wall along the draw direction are given in Fig. 2(a) with the corresponding radiation and convection heat fluxes in Fig. 2(b). The draw speed and glass/fiber radius are plotted along the draw direction in Fig. 2(c), which are normalized to the specified draw speed (25 m/s) and fiber radius (62.5 μm), respectively. Also graphed in Fig. 2(c) are the irradiation $\tilde{H}$ from the furnace and the heat-transfer coefficient $\overline{h}$ of the mixed air convection normalized to their respective maximum values listed in Table I.

Fig. 2(a)–(c) show that in the neck-down region inside the furnace (where the heating of the glass is dominated by radiation), q_c'' is negligible compared to q_r'', but it becomes significant in the post-chamber where the glass is primarily cooled by air convection due to the high surface area to volume ratio and the high moving speed of the glass.

Once the axial temperature distributions are obtained, the temperature-dependent coefficients of the PDEs can be computed using the properties of the glass, and its surrounding air given in Fig. 3(a) and (b). For completeness, the glass apparent emissivity is given as a function of optical thickness in Fig. 3(c), $\tau_{opt} = \alpha R(z)$ where α is the absorption coefficient in m^{-1} and $R(z)$ is the glass radius in meters.

Since the apparent irradiation $\tilde{H}(T)$ from the furnace in (1c) cannot be calibrated directly, we relate to the peak temperature

TABLE I
PARAMETERS USED IN THE SIMULATION

Specified values	Fiber radius, R_f (m)	62.5
	Draw tension, F_t (grams)	90
	Draw speed, v_f (m/s)	25
	Time constant of draw speed (s)	0.05
Preform	Radius, R_p (m)	0.045
	Time constant of feed-rate (s)	1
Furnace	Peak temperature, $T_{f,max}$(K)	2,400
	Minimum temperature, $_{f,min}$ (K)	1,700
	Radius, R_{fur} (m)	0.06
	Length, L_f (m)	0.45
	$\widetilde{H}_{max}$ (W/m^2)	1.58e6
Post-chamber	Radius, R_{post} (m)	0.055
	Length, L_p (m)	1.22
	$\overline{h}_{max}$ (W/m^2/K)	691
Glass Properties Fig. 3(a)	Density, ρ (kg/m^3)	2200
	Viscosity, μ (Pa·s)	
	$\mu(T) = 0.1\exp(-14.368 + 61{,}939.539/T$	[20]
	Thermal conductivity, k_m (W/m/K)	[21]
	Specific heat, C_p (J/kg/K)	[21]
	Apparent emissivity,	[21]
Air properties at 300K	Density, ρ (kg/m^3)	1.177
	Viscosity, μ (Pa·s)	1.983e-5
	Thermal conductivity, k_m (W/m/K)	0.026
	Specific heat, C_p (J/kg/K)	1005

T_f of the furnace so that the time constant of the furnace system in (19) can be characterized experimentally. Fig. 4 shows the simulated value of $\widetilde{H}$ to a step change in $T_f(= 0.015)$ along the z-axis at three different time instants during the transient. As shown in Fig. 4, the response is essentially static as the dynamic effect of radiosity from the glass on $\tilde{H}(T)$ is negligible. It is also noticed that the relative change of $\tilde{H}(T)$ in the furnace domain $(z < 0.45 \text{ m})$ is close to a constant. As the radiation heat flux is dominant only in the furnace domain, we consider the response of H in that region as a constant gain of $K = 0.06/0.015 = 4$. The time constant of the furnace dynamics is in the order of 3 min.

B. Validation of the ROM

As shown in Fig. 2(a) and (b), the glass flow is highly distributed along the draw direction. To complete the derivation of the ROM for the glass flow, we obtain numerically the snapshots using the nonlinear distributed quasi-1-D model. Although the dimension of the input space is infinite, it is not necessary to simulate all of the possible inputs since any arbitrary input function can be approximated by a corresponding Fourier transformed function with enough sinusoidal terms [12]. The ROM can be validated by comparing its solutions against the validated 2-D nonlinear distributed model of the draw process [17]. Two types of time functions were used in obtaining the snapshots; namely

1) step input of magnitude A;
2) sinusoidal function $A\sin(2\pi\omega_m t)$.

Since the bandwidths of the preform feedrate and the furnace radiation heating are small, only step responses are simulated. The type/value and the number of snapshots obtained for each input are given in Table II. Fig. 5 shows the first 20 eigenvalues of the matrix $\mathbf{B}$ in (9) for each of the state variables using a total of 754 snapshots. For each variable, the eigenvalues are
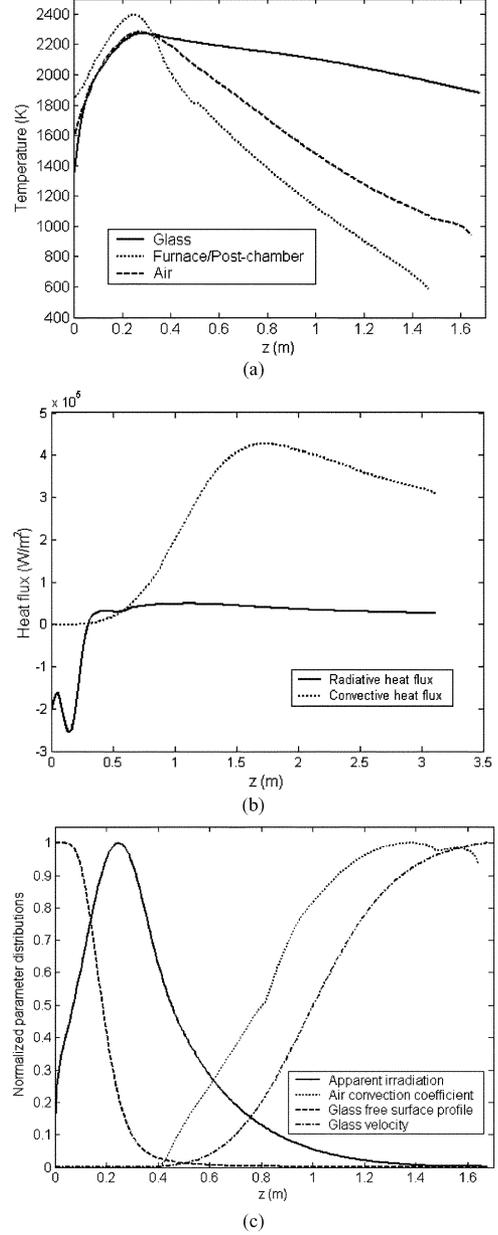
Fig. 2. Distributed variables and parameters at steady-state. (a) Axial temperature distributions. (b) Heat flux on the glass free surface. (c) Normalized parameters ($\widetilde{H}/\widetilde{H}_{max}$, $\overline{h}/\overline{h}_{max}$, R/R_f, v/v_f).

normalized to the first (maximum) one. These snapshots were used to solve for the eigenvectors in (9).

Neglecting the eigenmodes corresponding to small eigenvalues, we retain $N_a = N_v = N_T = 8$ eigenfunctions in deriving the ROM. Fig. 6 compared the step responses of the fiber diameter to a 4% change in v_f, 5% in v_p, and 2% in T_f. Each step response has been computed using three different models; namely, ROM, quasi-1-D and semi-2-D models. Since the actuator dynamics are well-defined ODEs, we exclude the actuator dynamics in Fig. 6. The comparisons show that the prediction of the 24th-order ROM to perturbations in draw speed and feedrate matches those computed using the nonlinear distributed models. Some discrepancy between the ROM (that closely follows the quais-1-D model from which it was derived) and the semi-2-D model can be explained as follows. The
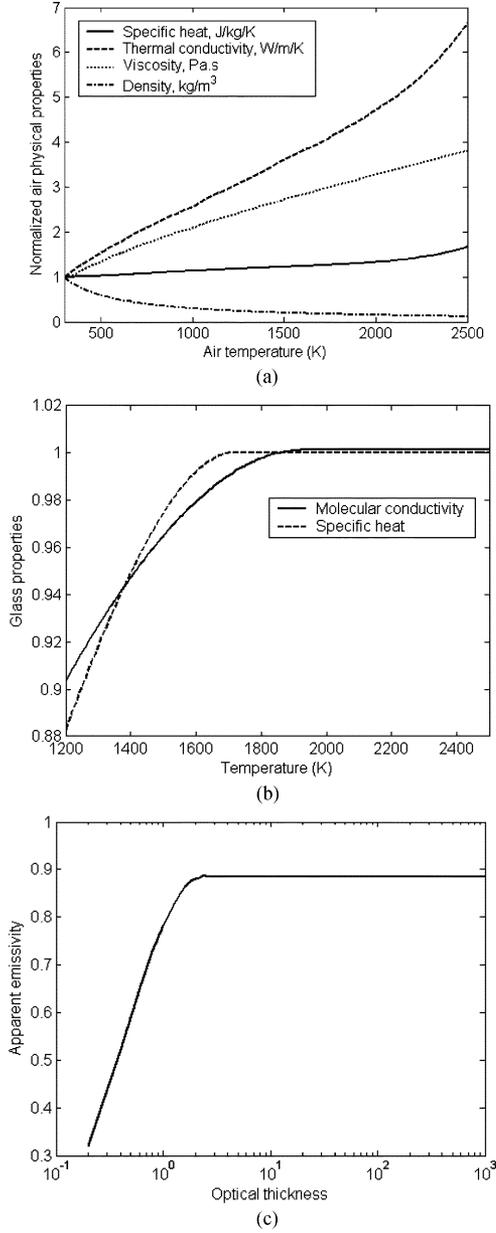
Fig. 3.   Properties of glass and air. (a) Air physical properties (normalized to values at 300 K). (b) Molecular thermal conductivity and specific heat of glass (normalized to values at the melting point of 1853 K, $k_m = 2.22$ W/m/K, $C_p = 1507$ J/kg/K). (c) Glass apparent emissivity.
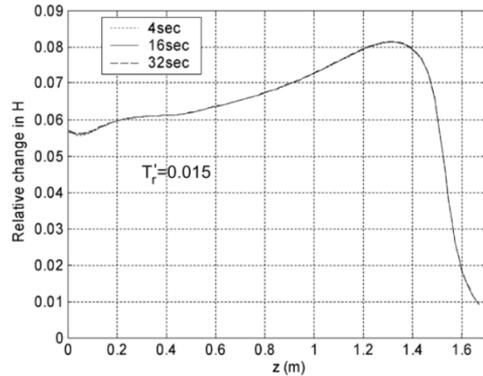
Fig. 4.   Step response of $\widetilde{H}(T)$ to a step change in $\hat{T}_f$.

Input variables	$\hat{v}_f(t)$	$\hat{v}_p(t)$	$\hat{T}_f(t)$	$\hat{h}(t)$
A	0.04	0.05	0.02	0.1
ω_m (Hz)	100	-	-	100
Number of snapshots	250	100	150	254
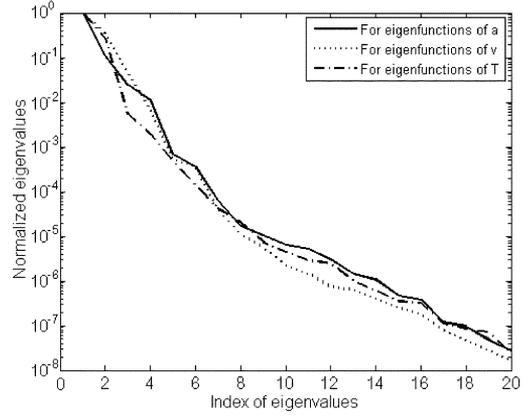
Fig. 5.   Normalized eigenvalues for snapshots.

heat input H appears explicitly in the energy equation of the quasi-1-D model, but indirectly through the furnace blackbody emissive power E_{bf} in the semi-2-D model. To approximately simulate the 2% step change in H, E_{bf} is increased by 2% in the semi-2-D simulation. Thus, the effective change in H for the semi-2-D simulation was less than 2% since H also includes the reflected radiosities originally from the preform, resulting in a slower response and a lower overshoot. It is expected that this slight model mismatch and the high-frequency noises in the air convection can be compensated using feedback control, which will be examined in the next section.

V. H∞/LQG CONTROL OF AN OPTICAL-FIBER DRAWING PROCESS

As an illustrative application, we consider here the control of an optical-fiber drawing process. The main sources of disturbances are the high-frequency noise due to the fluctuation in the convection heat-transfer coefficient h at the glass surface, and the change in the furnace temperature commonly used to regulate the tension of the fiber. We design an H∞/LQG controller, which not only minimizes the H$_2$ norm to guarantee the good performance of the closed-loop system but also reduces the H∞ norm to improve the system robustness to modeling errors. The objective is to keep the deviation of the fiber diameter within ± 0.5 μm of the nominal value 125 μm and as small as possible. At the same time, the temperature variation after leaving the post-chamber must be minimized to avoid downgrading the subsequent coating process. For this reason, the variations in draw speed must be kept within $\pm 1\%$ of the nominal value as small as possible; for a draw speed of 25 m/s, this corresponds to 0.25 m/s.
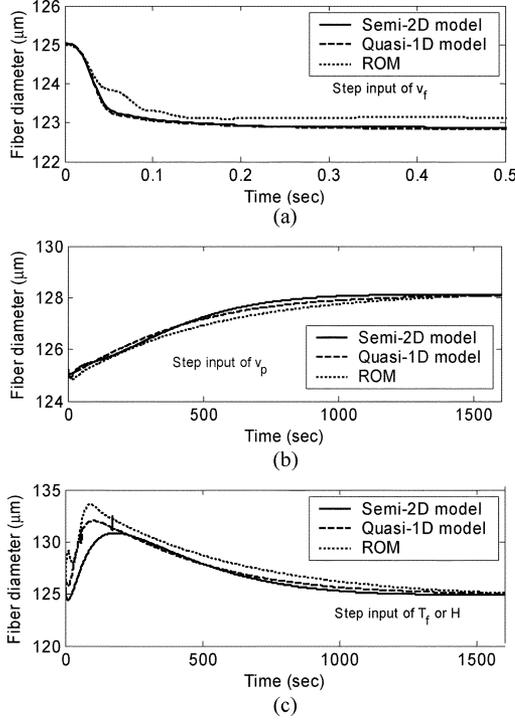
Fig. 6. Step responses of fiber diameter ($N_a = N_v = N_T = 8$). (a) Response to step change in draw speed. (b) Response to step change in feedrate. (c) Response to step change in furnace radiation.

A. Plant Model

The plant model is written in a standard state-space two-port system

$$\dot{\mathbf{x}} = \mathbf{A}\mathbf{x} + \mathbf{B}\mathbf{u} + \mathbf{D}_1\mathbf{w} \tag{23a}$$

$$\mathbf{y} = \mathbf{C}\mathbf{x} + \mathbf{D}\mathbf{u} + \mathbf{D}_2\mathbf{w} \tag{23b}$$

$$\mathbf{z} = \mathbf{E}_1\mathbf{x} + \mathbf{E}_2\mathbf{u} \tag{23c}$$

where $\mathbf{u}$ and $\mathbf{y}$ are input and output vectors defined in (19a) and (20), respectively; and $\mathbf{x}$ is the state vector (augmented with an integrator)

$$\mathbf{x} = [\mathbf{x}_0^T, \hat{v}_f, \hat{v}_p, \hat{T}_f, \hat{T}_a, x_{K+5}]^T \quad x_{K+5} = \int_0^t \hat{a}(L,t)dt$$

In (23a)–(b)

$$\mathbf{w} = [\mathbf{w}_1^T \quad \mathbf{w}_2^T]^T$$

where $\mathbf{w}_1$ is defined in (14b) and

$$\mathbf{w}_2 = [w_a \quad w_T \quad w_F]^T$$

accounts for heat flux fluctuations and sensor noises, respectively. The performance variable vector $\mathbf{z}$ in (23c) is given by

$$\mathbf{z} = [\mathbf{z}_x^T \quad \mathbf{z}_u^T]^T$$

$$\mathbf{z}_x = [x_{K+4} \quad \varepsilon_1\hat{F}(L,t)]^T$$

$$\mathbf{z}_u = \text{diag}([\varepsilon_2 \quad \varepsilon_3 \quad \varepsilon_4 \quad \varepsilon_5])\mathbf{u}$$
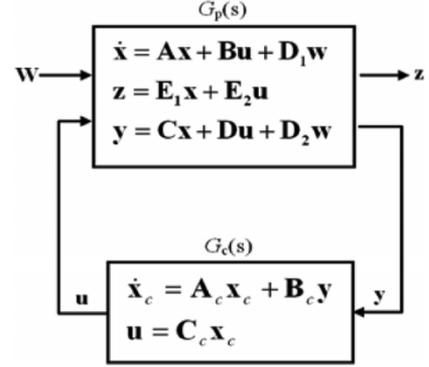
Fig. 7. Block diagram of the closed-loop system.

where $\varepsilon_i(i = 1, 2, 3, 4, 5)$ are the weights on the perfomance variables and control efforts. For the following simulation, we assign the fiber tension a lower control priority than the fiber diameter $\varepsilon_1 < 1$.

The matrices $\mathbf{A} \in \mathbf{R}^{(K+1)\times(K+1)}$, $\mathbf{B} \in \mathbf{R}^{(K+1)\times 4}$, and $\mathbf{C} \in \mathbf{R}^{2\times(K+1)}$ in (23a) and (23b) are readily obtained from (22)

$$\mathbf{A} = \left[\begin{array}{c|c} \mathbf{A}_0 & 0^{K\times 1} \\ \hline [1\ 0\ 0]\mathbf{C}_0 & 0 \end{array}\right]; \quad \mathbf{B} = \left[\begin{array}{c} \mathbf{B}_0 \\ 0^{1\times 3} \end{array}\right]$$

$$\mathbf{C} = [\mathbf{C}_0 \quad 0^{3\times 1}]; \quad \text{and} \quad \mathbf{D} = 0.$$

The weighting matrices for the input disturbances and sensor noise are given by

$$\mathbf{D}_1 = \left[\begin{array}{cc} \mathbf{D}_0 & 0^{K\times 3} \\ 0^{1\times 2} & 0^{1\times 3} \end{array}\right]; \quad \mathbf{D}_2 = \left[0^{3\times 2} \quad diag\left([\varepsilon_6 \quad \varepsilon_7 \quad \varepsilon_8]\right)\right]$$

where ε_i ($i = 6, 7, 8$) are the tunable weights accounting for the relative effects of the measuring noise. The weighting matrix $\mathbf{E}_1$ and $\mathbf{E}_2$ are defined as follows:

$$\mathbf{E}_1 = \left[\begin{array}{cc} 0^{1\times K} & 1 \\ [0\ 0\ \varepsilon_1]\mathbf{C}_0 & 0 \\ 0^{4\times(K+1)} & 0^{4\times 1} \end{array}\right]$$

$$\mathbf{E}_2 = \left[\begin{array}{c} 0^{1\times 4} \\ 0^{1\times 4} \\ \text{diag}\left([\varepsilon_2 \quad \varepsilon_3 \quad \varepsilon_4 \quad \varepsilon_5]\right) \end{array}\right].$$

B. $\text{H}\infty$/LQG Controller

As illustrated in Fig. 7, the control problem is to find $\mathbf{u}$ to regulate the fiber diameter under the effects of disturbances. For a stabilizable and detectable system given by (22), the mixed H_∞/LQG control problem is to determine a dynamic compensator

$$\dot{\mathbf{x}}_c = \mathbf{A}_c\mathbf{x}_c + \mathbf{B}_c\mathbf{y}$$

$$\mathbf{u} = \mathbf{C}_c\mathbf{x}_c \tag{24}$$

which satisfies the following design criteria:
  i) closed-loop system is internally stable;
  ii) closed-loop transfer function $\tilde{G}_{zw}(s)$ from disturbances $\mathbf{w}$ to performance variables $\mathbf{z}$ satisfies the constraint

$$\left\|\tilde{G}_{zw}(s)\right\|_\infty = \sup_{\omega \in \mathbf{R}} \sigma_{\max}\left[\tilde{G}_{zw}(j\omega)\right] \leq \gamma \tag{25}$$

where $\gamma > 0$ is a given small constant;
iii) the H_2 norm of $\tilde{G}_{zw}(s)$

$$\left\| \tilde{G}_{zw}(s) \right\|_2^2 = \frac{1}{2\pi} \int_{-\infty}^{\infty} \left\| \tilde{G}_{zw}(j\omega) \right\|_F^2 d\omega \qquad (26)$$

is minimized.

The solution of the $H\infty$/LQG control problem can be found in [22] and is given below

$$\mathbf{A_c} = \mathbf{A} - \mathbf{U}\mathbf{C}^T\mathbf{V}_2^{-1}\mathbf{C} - \mathbf{B}\mathbf{R}_2^{-1}\mathbf{B}^T\mathbf{P}(\mathbf{I} - \gamma^{-2}\mathbf{U}\mathbf{P})^{-1}$$
$$+ \gamma^{-2}\mathbf{U}\mathbf{R}_1 \qquad (27)$$
$$\mathbf{B_c} = \mathbf{U}\mathbf{C}^T\mathbf{V}_2^{-1} \qquad (28)$$
$$\mathbf{C_c} = -\mathbf{R}_2^{-1}\mathbf{B}^T\mathbf{P}(\mathbf{I} - \gamma^{-2}\mathbf{U}\mathbf{P})^{-1} \qquad (29)$$

where the positive semidefinite matrixes $\mathbf{P}$ and $\mathbf{U}$ satisfy

$$\mathbf{A}^T\mathbf{P} + \mathbf{P}\mathbf{A} + \left(\mathbf{E}_1^T\mathbf{E}_1\right) + \gamma^{-2}\mathbf{P}\mathbf{V}_1\mathbf{P}$$
$$- \mathbf{P}\mathbf{B}\left(\mathbf{E}_2^T\mathbf{E}_2\right)^{-1}\mathbf{B}^T\mathbf{P} = 0 \qquad (30)$$
$$\mathbf{A}\mathbf{U} + \mathbf{U}\mathbf{A}^T + \left(\mathbf{D}_1^T\mathbf{D}_1\right)\mathbf{V}_1 + \gamma^{-2}\mathbf{U}\mathbf{R}_1\mathbf{U}$$
$$- \mathbf{U}\mathbf{C}^T\left(\mathbf{D}_2^T\mathbf{D}_2\right)^{-1}\mathbf{C}\mathbf{U} = 0 \qquad (31)$$

where $\mathbf{R}_1 = \mathbf{E}_1^T\mathbf{E}_1$; $\mathbf{R}_2 = \mathbf{E}_2^T\mathbf{E}_2$; $\mathbf{V}_1 = \mathbf{D}_1^T\mathbf{D}_1$; and $\mathbf{V}_2 = \mathbf{D}_2^T\mathbf{D}_2$.

C. Results and Discussions

Simulations have been performed for the following studies.

Design I: $H\infty$/LQG Diameter Control Using Draw Speed Only: As shown in Fig. 6, the system responses to perturbations in v_p and T_f are very slow. It was found numerically and experimentally that manipulating the orifice opening to affect the air temperature could result in significant turbulent noise around the converging fiber and relatively large time-constant due to air capacitance in the post-chamber. Moreover, the operating range of the orifice opening is very small in order to ensure that the air is only exhausting from the post-chamber to the ambient to avoid contaminating the fiber. Thus, commercial draw processes often rely on manipulating the draw speed to control the fiber diameter. Using this, we investigate the effects of 1) the number of retained eigenmodes, and 2) modeling errors on the diameter uniformity.

Design II: $H\infty$/LQG Diameter Control Using Both Draw Speed and Air Temperature: Diameter control relying solely on manipulating the draw speed could adversely affect the subsequent coating process, which requires that the fiber be cooled to the room temperature before reaching the coating die. Moreover, the mechanical inertia of the rotating capstan/drum makes it difficult for the draw speed to respond quickly and accurately to high-frequency fluctuations such as w_h. We have observed numerically that changes in the air temperature surrounding the glass/fiber give rise to a rapid response to fiber diameter due to the strong temperature dependency of the glass viscosity. This finding is consistent with that observed experimentally by Imoto *et al.* [3]. Thus, we explore the effects of directly manipulating the gas temperature T_a, which can be changed by appropriately introducing a laminar gas flow around the glass/fiber surface as illustrated in Fig. 8.
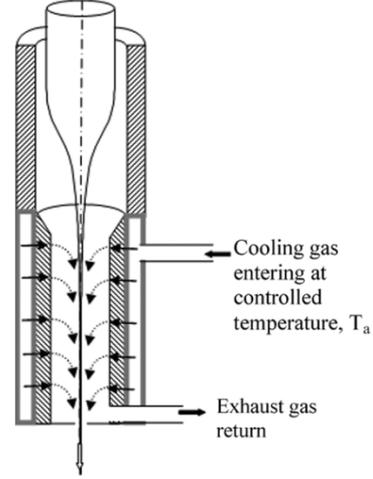
Fig. 8.   Schematics illustrating laminar cooling with T_a.

The values of the parameters used in the $H\infty$/LQG diameter controlled system are as follows:

Designs I and II

$\varepsilon_1 = 0.5$, $\varepsilon_3 = \varepsilon_4 = \varepsilon_5 = \varepsilon_6 = \varepsilon_7 = \varepsilon_8 = 0.001$

upper bound of $H\infty$ norm, $\gamma = 4.8$

$\tau_f = 0.05\,\text{s}$, $\tau_p = 1\,\text{s}$, $\tau_T = 180\,\text{s}$.

   Design I $\varepsilon_2 = 0.005$.

   Design II $\varepsilon_2 = 0.02$, $\tau_a = 0.01\,\text{s}$ (via laminar flow).

Equations (30) and (31) are solved using MATLAB.

Effects of the number of retained eigenmodes: In the attempt to optimize the performance of the $H\infty$/LQG diameter controlled system, we examine numerically the effects of the number of retained eigenmodes on the variations in fiber diameter and draw speed in the presence of high-frequency fluctuations in $\hat{h}$. The effects are studied by comparing the standard deviations (SDs) of the variations in fiber diameter D_f and draw speed v_f in the presence of a zero-mean white-noise with an SD of 2.13% and a maximum deviation (MD) of 8%. The model (with $N_a = N_v = N_T = 8$) is chosen here as a basis for comparison, where SD in D_f and v_f are 0.1901 μm and 0.4205 m/s, respectively. For $N_a \neq N_v \neq N_T$, the matrices in (22) can be derived by substituting perturbed state variables in (16a)–(c) into (15), and applying the Galerkin procedure detailed in Section III-3. The steps are tedious but relatively straightforward; they are not repeated here due to space limitations. Table III compares some example choices and their effects on the criteria. Two observations can be made.

1) When the total of retained eigenmodes (or the order of ROM) is doubled to 48th ($N_a = 30$, $N_v = 8$, and $N_T = 10$), the SD in draw speed is essentially doubled without significantly affecting the diameter variation. However, the closed-loop performance does not solely depend on the total number of retained eigenmodes.
2) For the same 24th order, the variations in fiber diameter can be reduced by approximately 25% without sacrificing the draw speed by appropriately distributing the number of retained eigenmodes.

In the following discussions, the 24th ROM with $N_a = 10$, $N_v = 8$, and $N_T = 6$ will be used in the $H\infty$/LQG diameter

TABLE III
EFFECTS OF THE NUMBER OF RETAINED EIGENMODES

N_a	30	20	10	10	10	10	10
N_v	8	8	8	12	4	8	8
N_T	10	10	10	10	10	20	6
$N_a+N_v+N_T$	48	38	28	32	24	38	24
SD D_f	0.16	0.15	0.13	0.14	0.14	0.17	0.14
v_f	0.85	0.89	0.65	0.43	0.57	0.68	0.43

TABLE IV
EFFECTS OF MODELING ERRORS ON ROBUSTNESS

Modeling error	SD of fiber diamerter (µm)	
	Open-loop	**Close-loop**
10% underestimation of $\bar{h}$	0.3531	0.1524
30K overestimation of T_f	0.3424	0.1397
10% underestimation of μ	0.3580	0.1387
50% underestimation κ_1	0.3475	0.1391
Combination of above errors	0.2735	0.1376

TABLE V
COMPARISON OF THREE CONTROL METHODS (TO WHITE NOISE
COUPLED 10% STEP INCREASE IN h)

Regulated variables	Standard Deviation		
	Open-loop	**CL without T_a control**	**CL with T_a control**
Fiber diameter	0.35µm	0.15µm	0.11µm
Fiber temperature	1.71K	1.47K	0.884K
Draw speed	NA	0.4685m/s	MD=0.156 m/s
Draw tension	0.80gram	2.33 gram	0.48 gram

control simulation. The minimum order is based on a numerical search by comparing the SD of the fiber diameter and the draw speed.

Effects of modeling errors: Table IV compares the SD of the fiber diameter in both the open-loop and the closed-loop responses to the same white noise in $\hat{h}(t)$ but under the influence of different modeling errors (in $\bar{h}$, T_f, μ, and the absorption coefficient at the small wavelength band κ_1). As shown in Table III, the H_∞/LQG control system reduces the SD in fiber diameter fluctuations to within 0.16 μm, less than 50% of the SD in the open-loop system.

Effects of air temperature manipulation: Three control methods are compared in response to a 10% step change in h superposed by a zero mean white-noise (2.13% SD, 8% MD):

1) open-loop with specified draw speed;
2) CL without T_a control: closed-loop $H\infty$/LQG diameter control with only draw speed manipulation;
3) CL with T_a control: closed-loop $H\infty$/LQG diameter control by controlling both the draw speed and the cooling gas temperature around the fiber.

The results are compared in Table V and the graphical responses of the fiber diameter, temperature, draw-speed, and tension are given in Fig. 9(a)–(d).

The comparisons in Table V show that the SD of the fiber diameter fluctuations can be reduced to 0.11 μm with negligible draw speed variations by controlling both the draw speed and air temperature (method C) which also exhibits excellent transient responses as compared to methods A and B as shown in Fig. 9. Fig. 9(d) shows that method B results in a much larger fluctuation in the fiber draw tension than that in methods A and C. It is because fiber tension depends significantly on the draw speed in
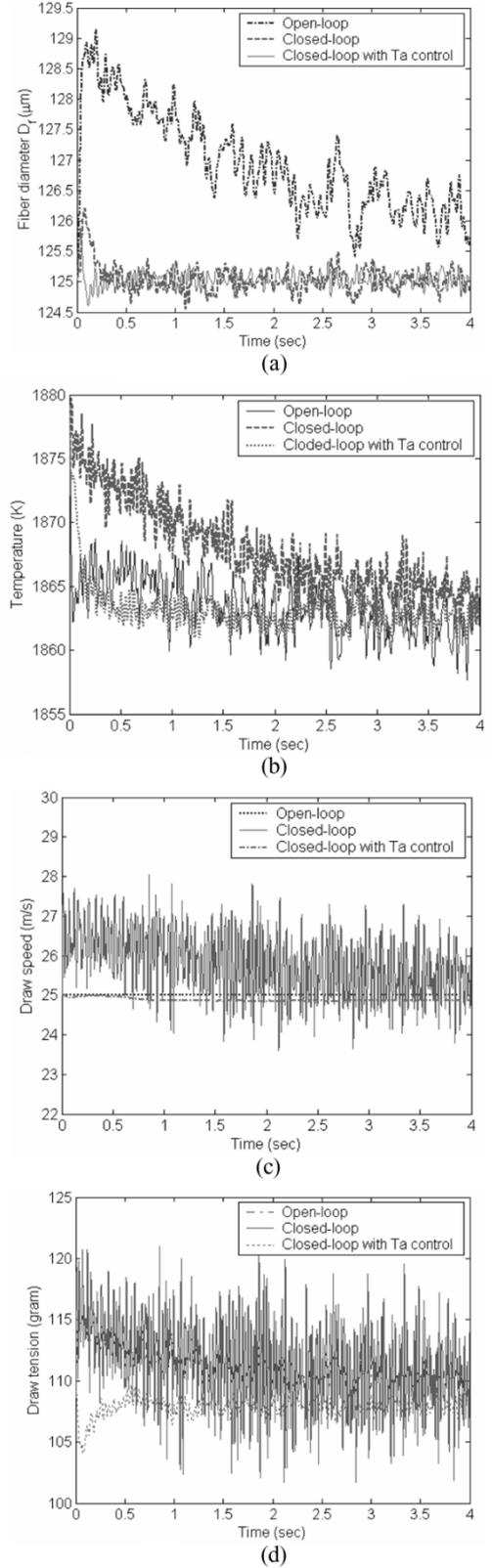
Fig. 9. Comparison of three control methods (to white noise coupled with a 10% step increase in h). (a) Responses of fiber diameter. (b) Response of the fiber temperature at the post-chamber exit. (c) Response of draw speed. (d) Responses of draw tension.

addition to the temperature-dependent viscosity and cross-section area of the glass fiber. Furthermore, the additional controlling input T_a eases the burden on the control effort in the draw

speed. Thus, the method of controlling both the air temperature T_a and the draw speed is very effective to regulate both fiber diameter and tension while simultaneously keeping the draw speed and temperature fluctuations to a minimum.

VI. Conclusion

We have presented a method to extend the Karhunen–Loeve decomposition technique with a Galerkin procedure to derive an ROM for a multivariable distributed-parameter system. The method has been numerically examined in the context of fiber diameter control of a modern draw tower capable of drawing fibers from large-diameter preform at high draw speed.

Perturbation studies have demonstrated that the 24th-order ROM agrees remarkably well with the original nonlinear semi-2-D and quasi-1-D distributed models. We further examine the efficiency of the ROM in the context of the model-based H_∞/LQG fiber drawing control system for the regulation of the fiber diameter and tension. The results show that variations in fiber diameter can be reduced significantly by appropriately distributing the number of retained eigenmodes among the physical state variables, and that controlling the surrounding air temperature in addition to the draw speed is very effective in regulating fiber diameter and tension simultaneously while keeping the draw speed and temperature fluctuations to a minimum.

It is expected that the modeling reduction techniques presented in this paper are applicable to other materials processing systems such as deposition thickness control in semiconductor manufacturing.

References

[1] M. Nakahara, S. Sakagauchi, and T. Miyashita, *Rev. Electr. Commun. Lab.*, vol. 26, pp. 476–483, 1978.

[2] D. H. Smithgall, "Application of optimization theory to the control of optical fiber drawing process," *Bell Syst. Tech. J.*, vol. 58, no. 6, pp. 1425–1435, 1979.

[3] K. Imoto, M. Sumi, G. Toda, and T. Suganuma, "Optical fiber drawing method with gas flow controlling system," *J. Lightwave Technol.*, vol. 7, pp. 115–121, 1989.

[4] A. Mulpur and C. Thompson, "Nonlinear control of optical fiber diameter variations," *IEEE Trans. Contr. Syst. Technol.*, vol. 4, no. 2, pp. 152–162, Mar. 1996.

[5] S. Tchikanda and K. M. Lee, "State space modeling of optical fiber drawing process," in *Proc. ACC*, Anchorage, AK, May 8–10, 2002.

[6] R. Temam, *Infinite-Dimensional Dynamical Systems in Mechanics and Physics*. New York: Springer-Verlag, 1988.

[7] M. Loeve, *Probability Theory*. Princeton, NJ: Van Nostrand, 1955.

[8] L. Sirovich and H. Park, "Turbulent thermal convection in a finite domain, part I: Theory," *Phys. Fluids A*, vol. 2, pp. 1649–1658, 1990.

[9] H. M. Park and D. H. Cho, "The use of the Karhunen-Loeve decomposition for the modeling of distributed parameter systems," *Chem. Eng. Sci.*, vol. 51, pp. 81–98, 1996.

[10] S. Banerjee, J. V. Cole, and K. F. Jensen, "Nonlinear model reduction of rapid thermal processing systems," *IEEE Trans. Semicon. Manufact.*, vol. 11, no. 2, pp. 266–275, May 1998.

[11] A. Theodoropoulou, R. A. Adomaitis, and E. Zafiriou, "Model reduction for optimization of rapid thermal chemical vapor deposition system," *IEEE Trans. Semicon. Manufact.*, vol. 11, no. 1, pp. 85–98, Feb. 1998.

[12] H. M. Park and M. W. Lee, "Boundary control of the navier-stokes equation by empirical reduction of modes," *Comput. Meth. Appl. Mech. Eng.*, vol. 188, pp. 165–186, 2000.

[13] J. Baker and P. D. Christofides, "Finite-dimensional approximation and control of nonlinear parabolic PDE systems," *Int. J. Contr.*, vol. 73, no. 5, pp. 439–456, 2000.

[14] A. Emami-Naeini, J. L. Ebert, D. De Roover, R. L. Kosut, M. Dettori, L. Porter, and S. Ghosal, "Modeling and control of distributed thermal systems," *IEEE Trans. Contr. Syst. Technol.*, vol. 11, no. 5, pp. 668–683, Sep. 2003.

[15] A. Tay, "Control of photoresist thickness uniformity in the microlithography process," in *Proc. Industrial Electronics Conf.*, vol. 3, 2003, pp. 2091–2096.

[16] Z. Y. Wei, K.-M. Lee, S. Tchikanda, Z. Zhou, and S.-P. Hong, "Free surface flow in high speed fiber drawing with large-diameter glass preforms," *ASME J. Heat Transf.*, vol. 126, no. 5, pp. 713–722, Oct. 2004.

[17] K.-M. Lee, Z. Wei, Z. Zhou, and S.-P. Hong, "Computational thermal fluid models for design of a modern fiber draw process," *IEEE Trans. Automat. Sci. Eng.*, vol. 3, no. 1, Jan. 2006.

[18] U. C. Paek and R. B. Runk, "Physical behavior of the neck-down region during furnace drawing of silica fibers," *J. Appl. Phys.*, vol. 49, pp. 4417–4422, 1978.

[19] L. Sirovich, "Turbulence and the dynamics of coherent structures," *Quart. Appl. Math.*, pt. I–III, vol. XLV, no. 3, pp. 561–571, 573-582, 583-590, 1987.

[20] N. P. Bansal and R. H. Doremus, *Handbook of Glass Properties*. New York: Academic, 1986.

[21] J. D. Fleming, "Final Report for the U.S. Atomic Energy Commission," Fused Silica Manual, Project no. B-153, Oak Ridge, TN, 1964.

[22] D. S. Bernstein and W. M. Haddad, Control-System Synthesis: The Fixed-Structure Approach, Lecture notes for the Robust Control graduate course in Georgia Tech., 1995.

Kok-Meng Lee (M'89–SM'02–F'05) received the B.S. degree from the State University of New York, Buffalo, in 1980, and the S.M. and Ph.D. degrees from the Massachusetts Institute of Technology, Cambridge, in 1982 and 1985, respectively.

Currently, he is a Professor in the Woodruff School of Mechanical Engineering at the Georgia Institute of Tecnology, Atlanta. His research interests include system dynamics/control, robotics, automation, and mechatronics. He holds eight patents in machine vision, three degrees of freedom (DOF) spherical motor/encoder, and live-bird handling system.

Dr. Lee is a Fellow of ASME. He received the National Science Foundation (NSF) Presidential Young Investigator, Sigma Xi Junior Faculty Research, International Hall of Fame New Technology, and Kayamori Best Paper awards.
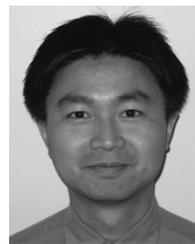
Zhiyong Wei received the B.S. and S.M. degrees in mechanical engineering from the Shanghai Jiao Tong University, Shanghai, China, in 1996 and 1999, respectively, and the Ph.D. degree in mechanical engineering from the Georgia Institute of Technology, Atlanta, in 2004.

Currently, he is a Computational Fluid Dynamics (CFD) engineer with Caterpillar, Inc., Mossville, IL, working on the development of new diesel engine components. His research interests are on computational modeling and control of dynamic thermal-fluid systems.

Zhi Zhou received the M.S. and B.S. degrees in electrical engineering from Jilin University of Technology, Changchun, China, in 1986 and 1983, respectively, and the Ph.D. degree in mechanical engineering from the Georgia Institute of Technology, Atlanta, in 1995.

Currently, he is a Manager with the Center of Excellence for Controls at Plug Power Inc., Latham, NY. Previously, he was a Technical Manager with Bell Laboratories of Lucent Technologies, formerly AT&T, Atlanta, GA, responsible for the optical-fiber draw technology research and development. His research interests include dynamic systems/controls, mechatronics, and fuel-cell systems. He holds nine U.S. patents.